

Effect of Annealing Atomic Rearrangement on Electrochemical Performance of Pd-Ni Catalyst

Liquan Lu^{1,#,*}, Shaofeng Yu^{2,#}, Xiuping Yue², Jing Wang¹, Meisheng Liang², Lizhen Gao², Shaohui Yan^{2,*}

¹ College of Mechatronic Engineering, North University of China, Taiyuan 030051, China

² College of Environmental Science and Engineering, Taiyuan University of Technology, Taiyuan, 030024, China

The first two authors contributed equally to this paper.

*E-mail: lq_lu@buaa.edu.cn; yanshaohui@tyut.edu.cn

Received: 5 April 2020/ Accepted: 6 June 2020 / Published: 10 July 2020

The rearrangement of the Pd and Ni atoms in the Pd-Ni nanoparticles is achieved by annealing under a vacuum condition with an absolute pressure of 0.03 MPa, to successfully synthesize carbon supported composite nanoparticles with Pd core and NiO_xH_y doped PdO shell (Pd@PdO-NiO_xH_y/C). This unique structure with a Pd core and a PdO metal oxide shell doped by NiO_xH_y is proved by the X-ray diffraction analysis and energy dispersive spectrometer mapping images. The shell structure of the Pd@PdO-NiO_xH_y nanoparticles is further proved by the X-ray photoelectron spectroscopy. The electrochemical test results indicate that the core-shell catalyst prepared at 400 °C (Pd@PdO-NiO_xH_y/C-400) catalyst has the best catalytic activities and stabilities in all the catalysts for the methanol electro-oxidation (MEO) and ethanol electro-oxidation (EEO). The peak value of the mass specific current density on the Pd@PdO-NiO_xH_y/C-400 catalyst for the MEO reaches to 1118.9 mA mg⁻¹ Pd, which is 2.5 and 1.4 times those of the Pd/C (443.1 mA mg⁻¹ Pd) and Pd-Ni/C (828.1 mA mg⁻¹ Pd) catalysts, respectively. This improvement is attributed to the unique doped structure between NiO_xH_y and PdO in the shell layer of the Pd-based nanoparticles in the core-shell catalyst, the promoting effect of the NiOOH, as well as the bifunctional mechanism. Under the influence of this doped structure, the new Pd nanoparticles generated by the rearrangement of the Pd atoms in the electrochemical activation process, are divided by the NiO_xH_y species, resulting in the new formed Pd nanoparticles have ultra-small size and high stability. These are also the reason that the Pd@PdO-NiO_xH_y/C-400 catalyst reveals good durability for both the MEO and EEO. Moreover, the ratio between its stable current densities for the EEO (86.35 mA mg⁻¹ Pd) and MEO (12.57 mA mg⁻¹ Pd) after 3600 s at -0.1 V vs. Ag|AgCl is 6.9, showing that the Pd@PdO-NiO_xH_y/C catalyst has broad application prospects in the field of the direct ethanol fuel cells.

Keywords: Direct Alcohol Fuel Cells; Methanol Electro-oxidation; Ethanol Electro-oxidation; Core-shell Structure; Pd based nanocatalyst; NiO_xH_y doped PdO.

1. INTRODUCTION

It is great important to improve the activity and durability of the electrocatalyst, for the commercial applications of the direct alcohol fuel cells (DAFCs). Although the Pt based nanocatalysts exhibit good electrocatalytic activity, their catalytic performances are still unsatisfactory [1-5]. In addition, the serious scarcity of the Pt resource has greatly frustrated their practical applications [6-9]. Therefore, it is urgent exploiting the non-platinum electrocatalyst with excellent activity, stability and efficiency [10-12]. Pd, as one replaced metal of Pt, has been extensively investigated in recent, due to their impressive catalytic activity and CO-tolerance ability for the methanol electro-oxidation (MEO) and ethanol electro-oxidation (EEO) in alkaline media [7,13-20].

Since the activity of the electrocatalyst strongly depends on its surface area, number of active sites and conductivity etc., many efforts have been made to optimize these characteristics for improving the electrocatalytic activity [21,22]. A general method is preparing bimetallic composite catalysts, because their active surface areas are increased by the synergistic structure between the two metals, which significantly enhances the activity and durability of the catalysts [23-26]. At present, numerous bimetallic Pd based catalysts, such as PdNi [7,13-16], PdCo [17], PdRu [18], PdCu [19], and PdAu [20], etc., have been employed widely in the anode electrocatalysts of the DAFCs. Among these Pd based electrochemical nanocatalysts, the Pd-Ni composite catalysts have attracted much attention, due to their excellent activity for many electrochemical reactions [7,13-16].

For the oxidation catalysis, oxygen reacts with the metal catalyst to produce a metal oxide layer on the surface of the catalyst, which represents a completely new compound compared to the original metal, and results in a significant enhancement in the catalyst performance [27]. The detailed information on the chemical properties of methanol on the clean and oxygen-modified transition metal surfaces has been reported in previous literatures [28-30]. The adsorbed oxygen atoms significantly enhance the chemical reactivity of the methanol oxidation on the transition surface, inducing a variety of oxidation reactions. The adsorbed oxygen atoms as a Bronsted base, stimulate the initial deprotonation of methanol to produce a methoxy intermediate with strong bonding force [30]. According to the mechanism that the redox reaction occurred at the surface of the oxides and oxyhydroxides, the reaction intermediates, OH and OOH, are attached on the surface active sites of the catalyst, which have a great improvement on the reaction kinetics [31-34]. Therefore, it is important to establish bonding sites for these intermediates. The aerobic properties of the metal oxides make the adsorbed OH species (OH_{ads}) be easily formed on their surfaces, improving the desorption rate of the intermediate products [35,36]. Therefore, it is a proper approach to establish a surface structure containing metal oxides, for improving the performance of the catalyst.

For increasing the amount of the metal oxides, the PtNi/C catalyst has been annealed at 200 °C under atmospheric conditions, which enhances the performance of the catalyst [37]. It has been reported that, moreover, the catalytic performances of numerous catalysts have been improved by the atomic rearrangement of the active nanoparticles in the catalyst caused by heat-treatment [37-40]. Furthermore, the atoms in the Pt-Ni nanoparticle catalysts are successfully rearranged by the electrochemical approach [41]. Therefore, it is great significant to research the effect of the atomic arrangement on the activity of the Pd-Ni catalyst for the MEO and EEO.

Here, the Pd and Ni atoms in the Pd-Ni/C (Pd-Ni composite nanoparticles supported on activated carbon) catalyst prepared by a polyol process are firstly rearranged by heat treatment to prepare the Pd@PdO-NiO_xH_y/C (Pd core NiO_xH_y doped PdO shell (Pd@PdO-NiO_xH_y) composite nanoparticles supported on activated carbon) catalyst. Then, the rearrangement of Pd atoms is achieved by the electrochemical activation to improve the performance of the Pd@PdO-NiO_xH_y/C catalyst. Furthermore, the effects of the atomic rearrangement on their structure, composition and electrocatalytic properties for the alcohol oxidation are studied in this work.

2. EXPERIMENTAL SECTION

2.1 Preparation of the Pd-Ni/C and Pd/C catalysts

The preparing process of the Pd-Ni/C catalyst is as follows. Firstly, the PdCl₂ solution is confected according to the method reported in literature [42]. Then, 48 mg activated carbon (Vulcan XC-72R) is dispersed in a mixed solution prepared by 2 ml 0.0564 M PdCl₂ solution, 0.5 ml 0.112 M NiCl₂ solution and 20 ml ethylene glycol using ultrasonic agitation for 25 min. Following by continue ultrasonic dispersion for 5 minutes, 6.8 ml 1 M KOH is added into the above solution. Subsequently, the mixture is transferred into a 100 ml stainless steel autoclave, and the small beaker is washed using 40 ml ethylene glycol solution, which is also transferred into the stainless steel autoclave. After the sealed container is heated from room temperature to 190 °C, it is held at this temperature for 6 hours and then naturally cooled to room temperature. The product is collected by filtering the mixture and washing repeatedly with ethanol and deionized water [43]. After the filter residue is dried in a vacuum oven at 80 °C for 6 hours, the Pd-Ni/C catalyst is prepared. In addition, the activated carbon support Pd nanoparticles (Pd/C) catalyst is prepared for comparison by the same preparation procedure as Pd-Ni/C without NiCl₂ solution is added.

2.2 Atomic rearrangement in the Pd-Ni/C catalyst

The atomic rearrangement in the Pd-Ni/C catalyst is achieved by annealing under a vacuum condition with an absolute pressure (P_{ABS}) of 0.03 MPa, which is carried out according to following steps. Firstly, the as-prepared Pd-Ni/C catalyst is placed in a tube furnace. Then, the air pressure is adjusted to 0.03 MPa using a vacuum pump. Subsequently, the Pd-Ni/C catalyst is annealed for 2 hours at 300, 400 or 500 °C, respectively. After the tube furnace is naturally cooled to room temperature, the Pd@PdO-NiO_xH_y/C catalyst is prepared, and taken out from the tube furnace. The Pd-Ni/C catalysts annealed at 300, 400 and 500 °C at vacuum condition are denoted as Pd@PdO-NiO_xH_y/C-300, Pd@PdO-NiO_xH_y/C-400 and Pd@PdO-NiO_xH_y/C-500, respectively. For comparison, the Pd-Ni/C catalyst is also annealed at 400 °C for 2 hours under the protection of a nitrogen atmosphere, which is indicated as Pd-Ni/C-400.

2.3 Physical characterization

The morphology and distribution of the Pd based nanoparticles in the catalysts are observed by a JEM 1200EX transmission electron microscope (TEM). The high-angle annular dark-field scanning TEM (HAADF-STEM) and energy dispersive spectrometer (EDS) mapping images of the Pd@PdO-NiO_xH_y nanoparticles in the Pd@PdO-NiO_xH_y/C-400 catalyst are collected using a Tecnai G2 F20 transmission electron microscope. The X-ray diffraction (XRD) data of the catalysts are recorded by a Bruker D8 Diffractometer. X-ray photoelectron spectroscopy (XPS) measurements are performed on a Thermo Scientific ESCALAB 250Xi XPS system. The loading of the metals in the catalysts are determined by Inductively Coupled Plasma-Mass Spectrometry (ICP-MS) using an Agilent 7500ce.

2.4 Electrochemical test

All electrochemical tests are performed using an electrochemical workstation (CHI760E, China), in a typical three-electrode system. A piece of graphite sheet (3 cm²) and an Ag|AgCl electrode are used as counter and reference electrodes, respectively. The preparing method of the working electrode is similar to the literatures [3,4,44,45]. Firstly, 10 μl catalyst inks, prepared using 1 mg catalyst, 0.95 ml water, 0.05 ml isopropanol and 30 μl 5% Nafion solution (Dupont Co., USA), are dropped on the surface of a glassy carbon electrode (Φ = 4 mm). Then, the inks are dried under the radiation of an infrared lamp for about 5-10 min. Before the electrochemical test, the electrolyte solution is blown by high purity nitrogen for 20 minutes to obtain O₂-free solution. The activity and stability of the catalyst are tested by cyclic voltammetry and chronoamperometry in 0.1 M KOH media respectively with 1 M CH₃OH and 1 M CH₃CH₂OH. For activating and calculating the electrochemical active surface area (ECSA) of the catalyst, the working electrode is firstly tested by cyclic voltammetry in a 0.05 M H₂SO₄ solution from -0.2 to 1.1 V at a scan rate of 50 mV s⁻¹, until the test curve is stable.

3. RESULTS AND DISCUSSION

3.1 Generation and evolution of the Pd@PdO-NiO_xH_y/C catalyst

Figure 1 shows the generation and evolution of the Pd@PdO-NiO_xH_y/C catalyst, from the synthesis of the Pd-Ni/C catalyst to the electrochemical activation of the Pd@PdO-NiO_xH_y/C catalyst. In this schematic diagram, the effect of the heat-treatment and electrochemical activation processes on the composition and structure of the activity nanoparticle in the catalyst is revealed, using a simple atomic model. For the preparation of the Pd/C and Pd-Ni/C catalysts, the catalyst precursors are reduced by the reducing species produced from the decomposition of ethylene glycol under a high temperature in alkaline medium [43].

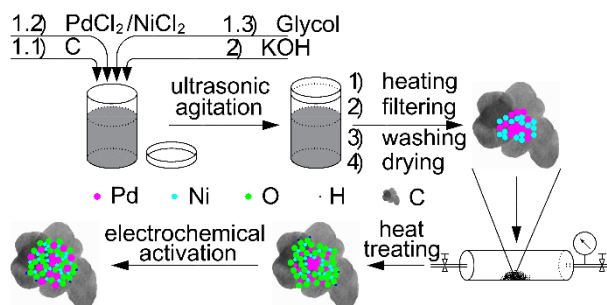
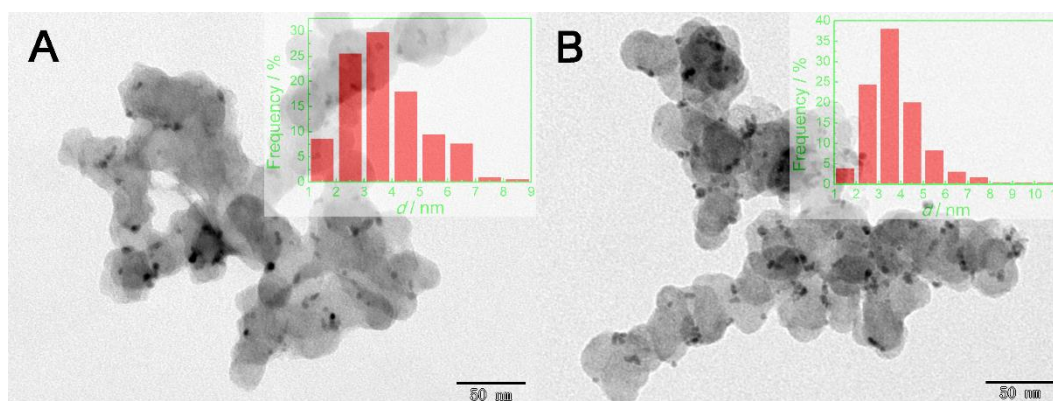


Figure 1. Schematic diagram about the generation and evolution of the Pd@PdO-NiO_xH_y/C catalyst from the synthesis of the Pd-Ni/C catalyst to the electrochemical activation of the Pd@PdO-NiO_xH_y/C catalyst.

3.2 Morphologies of the catalysts

Figure 2 reveals the TEM images of the as-prepared catalysts and their size distributions (inserts), which are obtained by a statistical approach [43-46]. Figure 2a and 2b present that the Pd based nanoparticles in the Pd/C and Pd-Ni/C catalysts are well dispersed on the carbon support. The particle diameter histograms in Figure 2 indicate that, the average diameters of the Pd based nanoparticles in the Pd/C, Pd-Ni/C, Pd-Ni/C-400, Pd@PdO-NiO_xH_y/C-300, Pd@PdO-NiO_xH_y/C-400 and Pd@PdO-NiO_xH_y/C-500 catalysts are about 3.73, 3.75, 4.09, 4.90, 5.06 and 6.66 nm, respectively. This result exhibits that the Pd based nanoparticles become big obviously due to the rearrangement of the Pd and Ni atoms, after the Pd-Ni/C catalyst is annealed. It is surprised that, however, the mean size of the Pd@PdO-NiO_xH_y nanoparticles in the Pd@PdO-NiO_xH_y/C-400 catalyst is much larger than that of the Pd-Ni nanoparticles in the Pd-Ni/C-400 catalyst. This phenomenon is resulted from the insertion of the O atoms in the crystal lattice of the Pd-Ni nanoparticles to form metal oxides, due to the reaction between the metal and oxygen. Therefore, the rearrangements of the Pd and Ni atoms are accelerated with the assistance of O₂. The corresponding evolution process is displayed in Figure 1. For the Pd@PdO-NiO_xH_y/C catalyst, the average diameter of the Pd@PdO-NiO_xH_y nanoparticles increases with the annealing temperature, implying that the annealing temperature is another factor affecting the atomic rearrangement level.



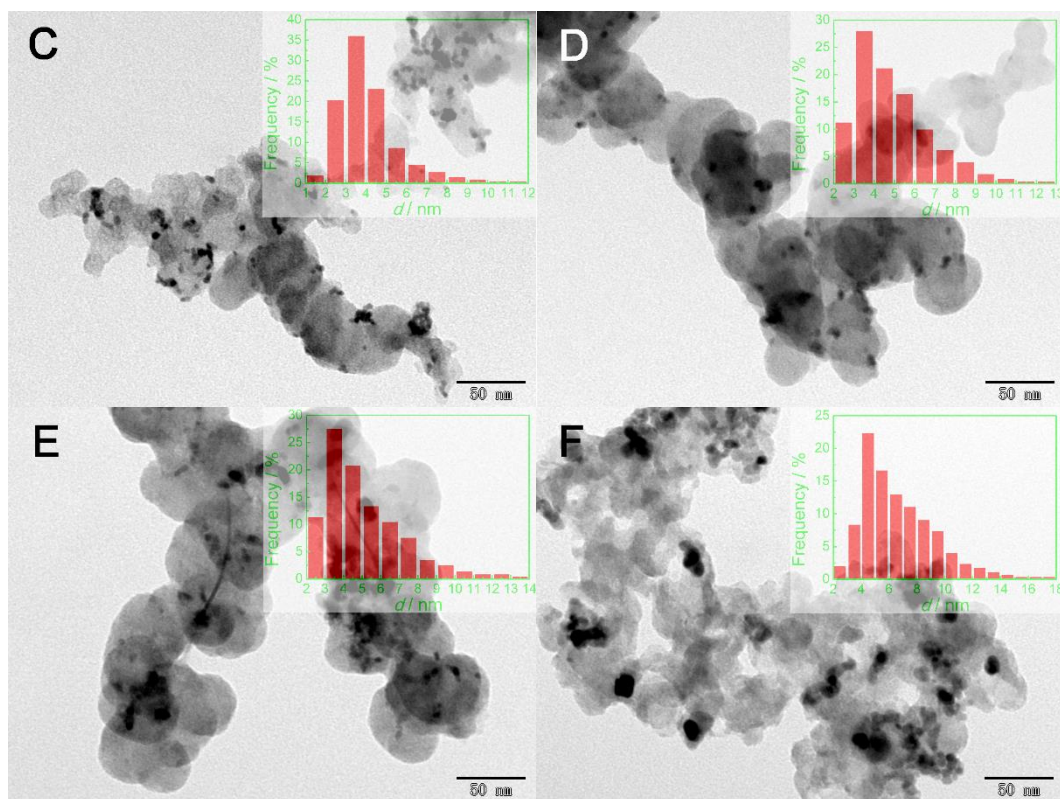


Figure 2. TEM images of the Pd/C (A), Pd-Ni/C (B), Pd-Ni/C-400 (C), Pd@PdO-NiO_xH_y/C-300 (D), Pd@PdO-NiO_xH_y/C-400 (E), and Pd@PdO-NiO_xH_y/C-500 (F) catalysts. Inserts show the corresponding particle diameter histogram.

3.3 Compositions of the catalysts

Table 1. Metal loading of the catalysts measured by ICP-MS

| Catalyst | Pd loading (wt%) | Ni loading (wt%) | Actual total Metal loading (wt%) | Theoretical total metal loading (wt%) |
|---|------------------|------------------|----------------------------------|---------------------------------------|
| Pd/C | 27.4 | NA | 27.4 | 30.0 |
| Pd-Ni/C | 16.0 | 2.2 | 18.2 | 24.1 |
| Pd-Ni/C-400 | 15.5 | 3.3 | 18.8 | 24.1 |
| Pd@PdO-NiO _x H _y /C-300 | 14.2 | 2.6 | 16.8 | 24.1 |
| Pd@PdO-NiO _x H _y /C-400 | 15.9 | 3.2 | 19.1 | 24.1 |
| Pd@PdO-NiO _x H _y /C-500 | 53.4 | 9.5 | 62.9 | 24.1 |

The Pd and Ni loadings of the catalysts tested by ICP-MS are listed in Table 1. The theoretical Pd and Ni loadings in the bimetallic catalyst are 18.9% and 5.2%, respectively. However, the actual Pd and Ni loadings of the Pd-Ni/C catalyst respectively are about 16.0% and 2.2%, which are both lower than the corresponding theoretical values, especially for the Ni loading. This is caused by the incomplete reduction of the precursor [43]. However, the actual Pd and Ni loadings of the Pd@PdO-

NiO_xH_y/C-500 are far higher than their theoretical loadings, reaching to about 53.4% and 9.5%. The possible reason is the activated carbon reacted with oxygen when the Pd-Ni/C is annealed at 500 °C, leading to a great loss for the carbon support.

3.4 Structure of the Pd@PdO-NiO_xH_y/C catalysts

Figure 3 indicates the XRD profiles of the Pd/C, Pd-Ni/C, Pd-Ni/C-400, Pd@PdO-NiO_xH_y/C-300, Pd@PdO-NiO_xH_y/C-400 and Pd@PdO-NiO_xH_y/C-500 catalysts. In Figure 3, the diffraction peak at 25.4° is assigned to the C (002) plane of the carbon support [JCPDS, No. 74-2330] [43,44,46]. For the Pd/C catalyst, the peaks at 40.1, 46.6, 68.5 and 82.3° correspond to the (111), (200), (220) and (311) planes of Pd with fcc structure [JCPDS, No. 5-0681], respectively [47]. Compared to the Pd/C catalyst, the positions of the peaks in the Pd-Ni/C diffraction pattern hardly shift, indicating that the Pd-Ni alloy phase is not easily formed under the preparation conditions. However, the Pd (111), (200), (220) and (311) crystal planes of the Pd-Ni/C-400 catalyst in Figure 3 are respectively located at 40.6, 46.9, 68.8 and 82.7°, which are between the 2θ values of the pure Pd and pure Ni [JCPDS, No. 4-0850]. This phenomenon indicates that some Ni atoms enter the lattice of the Pd nanoparticles and partially replace the Pd atoms. Therefore, the Pd-Ni alloy phase is formed, and the lattice parameters of the Pd crystals are changed due to the electron-inducing effect of the Ni atoms on Pd atoms [48]. This change in the lattice parameters of noble metals can significantly enhance its catalytic activity [49]. The Pd@PdO-NiO_xH_y/C-300, Pd@PdO-NiO_xH_y/C-400 and Pd@PdO-NiO_xH_y/C-500 catalysts exhibit great different diffraction peaks, compared to the Pd/C, Pd-Ni/C and Pd-Ni/C-400 catalysts. The strong diffraction peaks at 33.8, 41.9, 54.7, 60.2 and 71.4° are related to the (101), (110), (112), (103) and (202) planes of PdO [JCPDS, No. 75-0584], respectively [50]. In addition, the peaks corresponding to the Pd (111) plane are situated at about 40.1°, although it is extremely weak. These results suggest that most of the Pd atoms in the Pd@PdO-NiO_xH_y/C catalysts are principally PdO, and only few Pd atoms are existed as metallic Pd. It is preliminarily concluded that, therefore, the outer Pd atoms in the Pd-Ni/C catalysts are oxidized to form the PdO shell layer, when it is annealed in the tube furnace with the vacuum degree of 0.07 MPa; while a small part of inner Pd atoms are still the metallic Pd. Namely, the Pd@PdO-NiO_xH_y nanoparticles have a core-shell structure. Moreover, the Pd (111) diffraction peaks of the Pd@PdO-NiO_xH_y/C catalysts scarcely shift with the increase in the heating temperature, which suggests that no metallic Ni exists in these catalysts. Or else, the Pd (111) diffraction peaks will shift to the high 2θ value with the enhancement in the heating temperature, which is similar to the result that the Pd diffraction peaks of the Pd-Ni/C-400 catalyst has higher 2θ value than the Pd-Ni/C catalyst. Therefore, the metallic Ni atoms hardly exist in the Pd@PdO-NiO_xH_y/C catalysts. In other words, all the Ni atoms in the Pd@PdO-NiO_xH_y/C catalysts appear to be the oxidized form (NiO_xH_y). Compared to the standard XRD card of PdO, the diffraction peaks of the PdO shell layer in the Pd@PdO-NiO_xH_y/C catalysts scarcely shift, meaning that the PdO shell layer in these catalysts is pure PdO. Therefore, no new phase is formed between PdO and NiO_xH_y. This result suggests that the oxidation of the Pd and Ni atoms in the annealing process makes the Pd-Ni nanoparticles in the Pd-Ni/C catalyst are turned into the Pd@PdO-NiO_xH_y nanoparticles in the Pd@PdO-NiO_xH_y/C catalyst. During this

procedure, the Pd and Ni atoms are inevitably rearranged according to the related sketch map shown in Figure 1. Furthermore, the diffraction peaks of both Ni and NiO_xH_y are never found in the XRD patterns of all the Pd based catalysts. The possible reason is that Ni and NiO_xH_y in the composite nanoparticles are existed as an amorphous form. This structure can fully utilize the merits of the NiO_xH_y species with excellent co-catalysis effect to prompt the catalytic performance of the Pd@PdO- NiO_xH_y /C catalyst.

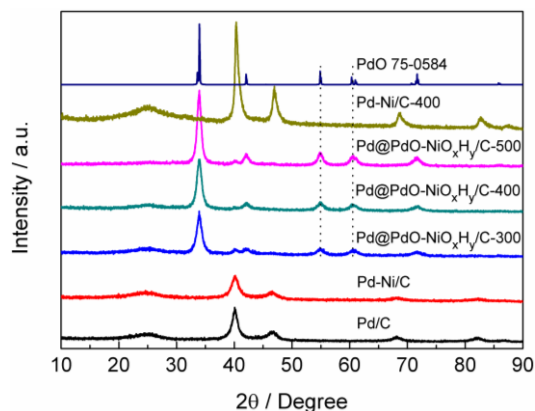


Figure 3. XRD profiles of the Pd/C, Pd-Ni/C, Pd-Ni/C-400, Pd@PdO- NiO_xH_y /C-300, Pd@PdO- NiO_xH_y /C-400 and Pd@PdO- NiO_xH_y /C-500 catalysts. The standard XRD card of PdO is included for reference.

To further identify the core-shell structure, and study the distributions of the Pd, Ni, and O components of the Pd@PdO- NiO_xH_y nanoparticles, the Pd@PdO- NiO_xH_y /C-400 catalyst is investigated using an EDS mapping analysis in the HAADF-STEM mode. The HAADF-STEM and EDS mapping images of the Pd@PdO- NiO_xH_y nanoparticles in the Pd@PdO- NiO_xH_y /C-400 catalyst are shown in Figure 4. The pink, blue, and green points represent the Pd, Ni, and O elements, respectively. Compared the HAADF-STEM image with the EDS mapping images of the Pd, Ni and O elements, it is found that, the outline of their distributions very similar. To obtain more detailed information, the mixed EDS mapping images of the Pd and Ni elements, and the Pd, Ni and O elements are shown in Figures 4E and 4F, respectively. It can be seen clearly from Figure 4E that, some Ni atoms are primarily distributed on the edge of the Pd@PdO- NiO_xH_y nanoparticles, which is shown by a green rectangle; while some Ni atoms in some region (orange oval-shaped area) reveal relatively uniform. This phase separation phenomenon is caused by the clustering phenomena or spinodal decomposition [45]. According to Figures 4B, 4C, 4D and 4E, the O atoms are mainly distributed near the Ni elements. The possible reason is that the oxygen level in NiO_xH_y is higher than that in PdO. These results further suggest that, both the Ni and Pd elements on the surface of the Pd@PdO- NiO_xH_y nanoparticles are oxidized by O_2 to respectively form PdO and NiO_xH_y . Figure 4F indicates that, only few O atoms are distributed in the two regions denoted by white dotted circles compared to the adjacent regions. This implies that the Pd cores of the Pd@PdO- NiO_xH_y nanoparticles are located at these regions, which is mainly situated in the phase separation zone. However, the O atoms are distributed throughout the other regions of the Pd@PdO- NiO_xH_y nanoparticles, showing that PdO and NiO_xH_y are evenly mixed together to form a unique doped structure, in the shell layers of the

Pd@PdO-NiO_xH_y nanoparticles and the regions that the Pd and Ni atoms are uniformly distributed.

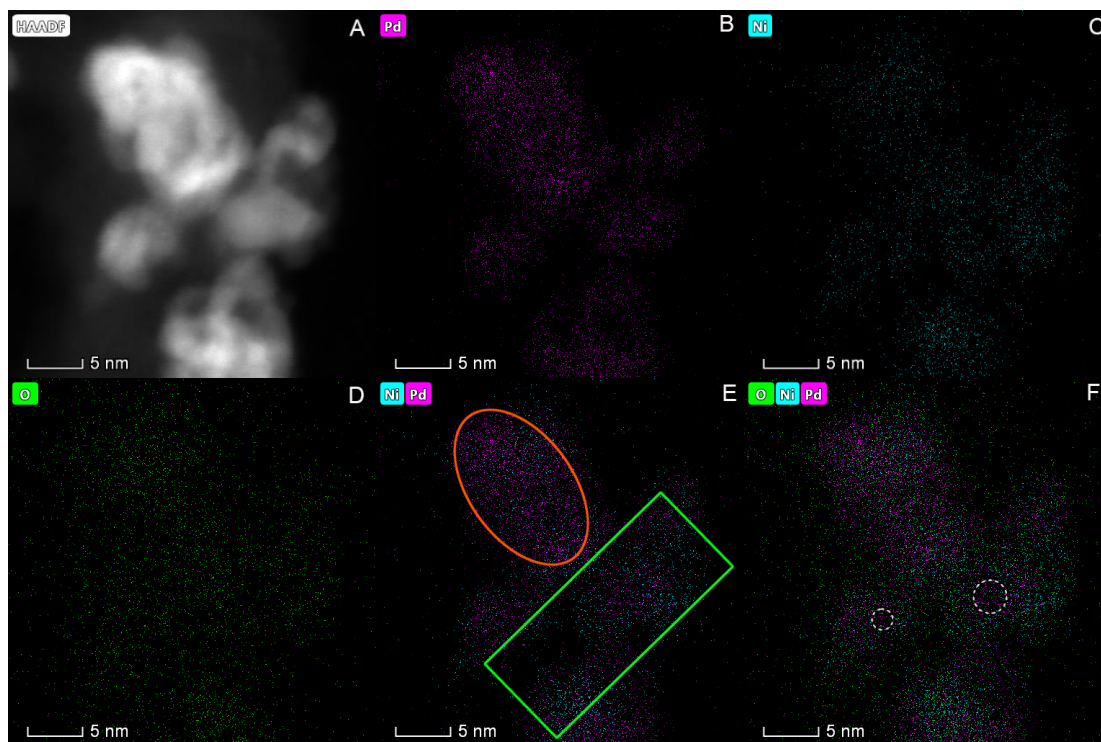


Figure 4. HAADF-STEM (A) and EDS mapping images (B–F) of the Pd@PdO-NiO_xH_y nanoparticles in the Pd@PdO-NiO_xH_y/C-400 catalyst.

The chemical states of the surface Pd and Ni atoms in the Pd@PdO-NiO_xH_y/C-400 catalyst are determined by an XPS analysis. The total spectrum of the Pd@PdO-NiO_xH_y/C-400 catalyst is depicted in Figure 5A, which contains a C 1s peak at 284 eV, an O 1s peak at 531 eV, a Pd 3d peak at 337 eV, and a Ni 2p peak at 855 eV. The most intense peak in the C 1s spectrum (Figure 5B) is located at 284.79 eV, which is very close to 284.80 eV of pure carbon [51]. The inferior and weak doublets around 286.28 and 288.82 eV represent C-O and C=O, respectively [51]. The narrow scan spectrum of Ni 2p (Figure 5C) shows a complex structure, in which spin-orbit coupling is found in the Ni 2p spectrum, and shake-up peaks appear at 861.4 and 880.8 eV, due to the multi-electron excitation [52]. Considering the shake-up peaks, Ni 2p_{3/2} decomposes into four peaks at 854.26, 855.34, 856.43 and 857.30 eV, which respectively correspond to NiO, Ni(OH)₂, NiOOH and Ni₂O₃ [45,53-55]. No metallic Ni peak is found in the Ni 2p spectrum at about 852.3 eV, which further proves that all the Ni atoms in the Pd@PdO-NiO_xH_y/C-400 catalyst are fully oxidized [45]. Due to spin-orbit coupling, the Pd 3d spectrum shown in Figure 5D is mainly divided into two parts: a low binding energy band at 337.27 eV (Pd 3d_{5/2}) and a high binding energy band at 342.63 eV (Pd 3d_{3/2}), which both correspond to PdO [51,56-58]. The other two weak peaks located at 339.70 and 345.34 eV are associated to the PdO₂ [56]. Surprisingly, the metallic Pd signal never appears at about 335.2 eV in the XPS spectrum [51,56-58], which is different to the XRD result (the metallic Pd is found in the profile of the Pd@PdO-NiO_xH_y/C

catalysts), further indicating that the metallic Pd is located at the center of the Pd@PdO-NiO_xH_y nanoparticle to form the pure metallic Pd core. Moreover, it is wrapped by NiO_xH_y doped PdO to form core-shell structure.

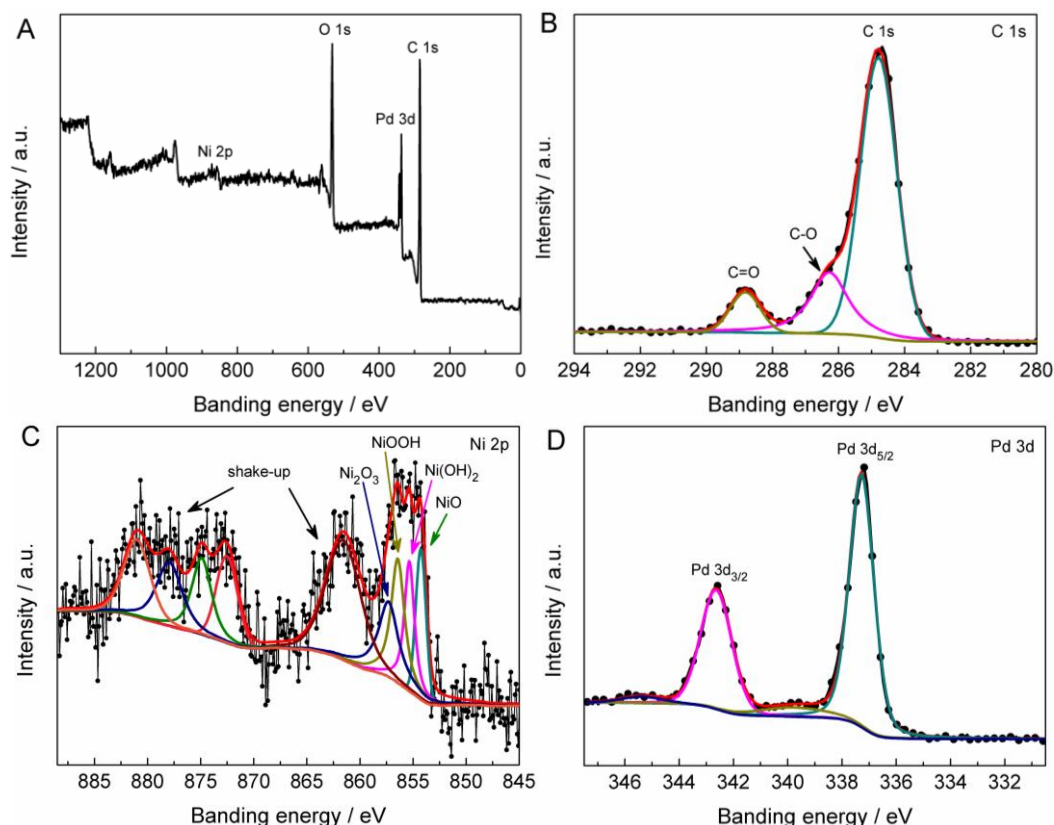


Figure 5. XPS spectra of the Pd@PdO-NiO_xH_y/C-400 catalyst in the total (A), C 1s (B), Ni 2p (C) and Pd 3d (D) regions.

3.5 Electrochemical test

Figure 6A shows the cyclic voltammograms (CVs) on the as-prepared catalysts in a 0.05 M H₂SO₄ electrolyte at a scan rate of 50 mV s⁻¹, in a scan potential range of -0.2 to 1.1 V vs. Ag|AgCl. In the hydrogen region between -0.2 and 0.1 V, a hydrogen adsorption/desorption process is performed [51]. The potential range from 0.1 to 0.5 V is an electric double layer region [59]. The Pd oxidized and oxygen evolution regions respectively are 0.5 to 1.0 V, and 1.0 to 1.1V [59]. The current peak appearing at 0.1-0.7 V during the negative scanning is attributed to the reduction of PdO to Pd, which is usually used to evaluate the ECSA of the catalyst, according to a value of 405-420 μC cm⁻² [58,60]. The calculated ECSAs according to the PdO reduction zone for the Pd/C, Pd-Ni/C, Pd-Ni/C-400, Pd@PdO-NiO_xH_y/C-300, Pd@PdO-NiO_xH_y/C-400 and Pd@PdO-NiO_xH_y/C-500 catalysts are 347.1, 836.2, 489.5, 990.5, 1071.9 and 110.5 cm² mg⁻¹ Pd, respectively. The Pd@PdO-NiO_xH_y/C-500 catalyst exhibits the smallest ECSA, due to big size of the Pd@PdO-NiO_xH_y nanoparticles, which is caused by the excessive oxidation of the Pd and Ni components. The Pd@PdO-NiO_xH_y/C-400 catalyst reveals the largest ECSA among these catalysts, which is 3.1 and 1.3 times the ECSAs of the Pd/C and Pd-Ni/C

catalysts, respectively. The initial 3 CVs on the Pd/C and Pd@PdO-NiO_xH_y/C-400 catalysts in 0.05 M H₂SO₄ solution are indicated in Figure 6B, which reveals that the current peak related to the PdO reduction increases with the number of scanning cycles, suggesting that the ECSA is constantly enhanced during the electrochemical activation process. However, the ECSA of the Pd@PdO-NiO_xH_y/C-400 catalyst increases much faster compared to the Pd/C catalyst. This phenomenon implies that, the great enhancement in the ECSA of the Pd@PdO-NiO_xH_y/C-400 catalyst is caused by more than just the electrochemical cleaning of its surface. The formation of the new Pd nanoparticles caused by the atomic rearrangement during the reduction process of PdO is a key factor. The corresponding schematic drawing is indicated in Figure 1. As the number of scanning cycles increases, in addition, more and more PdO species are electrochemically reduced to form the Pd nanoparticles in the shell layer of the Pd@PdO-NiO_xH_y nanoparticles. Obviously, these newly generated metallic Pd nanoparticles determine the electrochemical performances of the Pd@PdO-NiO_xH_y/C catalyst. Due to the doped shell structure between PdO and NiO_xH_y in Pd@PdO-NiO_xH_y nanoparticles, the rearrangement of the Pd atoms is restricted by the NiO_xH_y species during the reduction procedure of the PdO species in the electrochemical activation procedure. Therefore, the new Pd nanoparticles are separated by the NiO_xH_y species, causing the newly formed Pd nanoparticles have ultra-small size. Therefore, the newly produced Pd nanoparticles with small size result in both the Pd@PdO-NiO_xH_y/C-300 and Pd@PdO-NiO_xH_y/C-400 catalysts have large ECSA, due to the size effect [46]. According to the CVs at the region from 0.5 to 1.1 V shown in Figure 6B, the mass-specific current densities of the anodic polarization curve on the Pd@PdO-NiO_xH_y/C-400 catalyst enhances with the cycling number increasing, as well as the CVs exhibit the characteristics of the metallic Pd after the first scan cycle, which is in complete agreement with the previous report [61]. This proves again that a large amount PdO in the shell layer of the Pd@PdO-NiO_xH_y nanoparticles is reduced to form the metallic Pd after the first CV scan. Otherwise, a few NiO_xH_y components may be dissolved in the H₂SO₄ solution during the electrochemical activation process, leading to the surface of the Pd@PdO-NiO_xH_y nanoparticles form a porous structure like the literatures [38,41]. This structure makes many newly formed Pd nanoparticles exist as an island, which is another possible reason that makes the Pd@PdO-NiO_xH_y/C-400 catalyst has large ECSA. Comparing to the Pd/C catalyst, furthermore, the addition of Ni in the Pd-Ni/C catalyst increases its ECSA, because the Ni element promotes the surface segregation of the Pd atoms in the catalyst. The reason that the ECSA of the Pd-Ni/C-400 catalyst is considerably decreased compared to the Pd-Ni/C catalyst, may be caused by the increase in the average size and the formation of the Pd-Ni alloying phase [62,63].

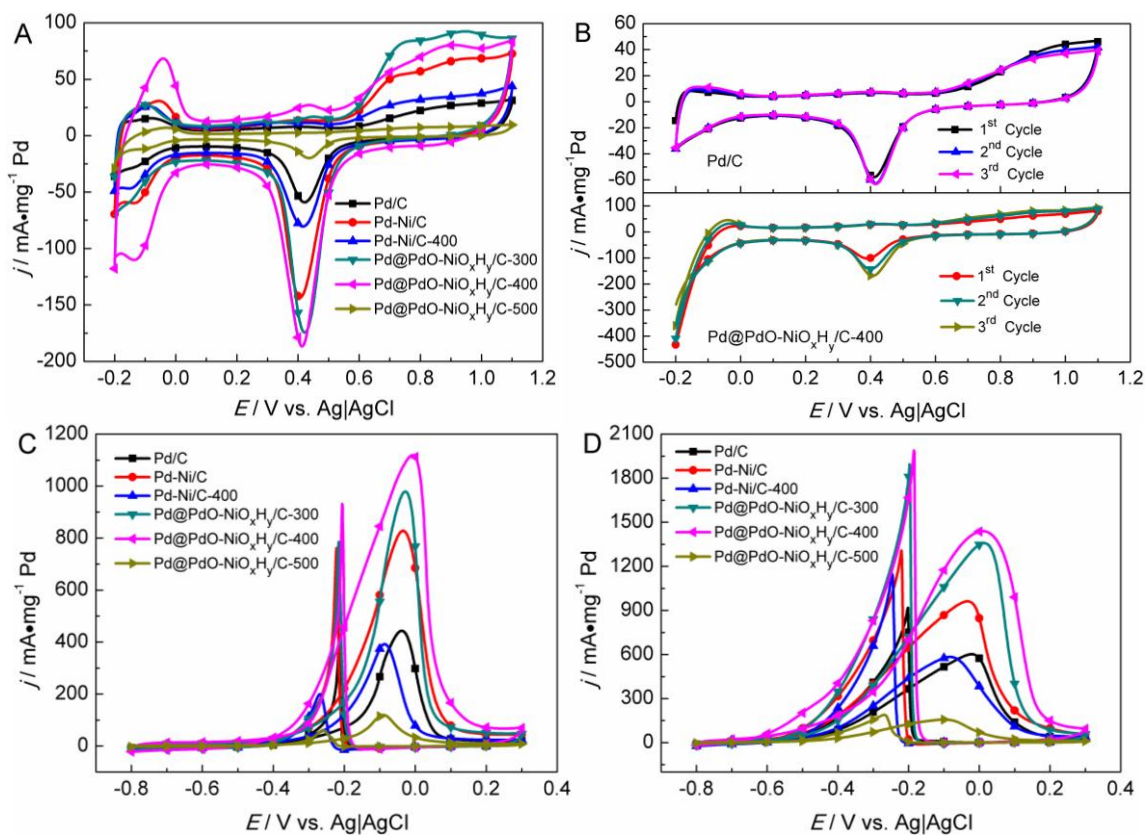
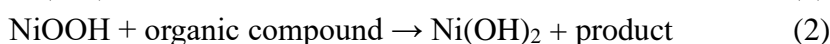


Figure 6. (A) CVs of the Pd/C, Pd-Ni/C, Pd-Ni/C-400, Pd@PdO-NiO_xH_y/C-300, Pd@PdO-NiO_xH_y/C-400 and Pd@PdO-NiO_xH_y/C-500 catalysts in 0.05 M H₂SO₄ between -0.2 and 1.1 V. (B) CVs of the Pd/C and Pd@PdO-NiO_xH_y/C-400 catalysts in 0.05 M H₂SO₄ between -0.2 and 1.1 V from 1st to 3rd cycle. CVs of alcohol oxidation on the Pd/C, Pd-Ni/C, Pd-Ni/C-400, Pd@PdO-NiO_xH_y/C-300, Pd@PdO-NiO_xH_y/C-400 and Pd@PdO-NiO_xH_y/C-500 catalysts in 0.1 M KOH + 1 M CH₃OH (C) and 0.1 M KOH + 1 M CH₃CH₂OH (D) mixed solutions. Scan rate: 50 mV s⁻¹. All the currents are normalized using the Pd loading determined by ICP-MS.

Figures 6C and 6D are the CVs on the Pd/C, Pd-Ni/C, Pd-Ni/C-400, Pd@PdO-NiO_xH_y/C-300, Pd@PdO-NiO_xH_y/C-400 and Pd@PdO-NiO_xH_y/C-500 catalysts respectively in 0.1 M KOH + 1 M CH₃OH and 0.1 M KOH + 1 M CH₃CH₂OH mixed solutions at a scan rate of 50 mV s⁻¹. In Figure 6C, the peaks near 0 V in the forward scan are related to the MEO, and the sharp peaks appearing about -0.2 V in the reverse scan are resulted from the electro-oxidation of the carbonaceous species, which is produced and adsorbed on the electrode surface during the forward scan, such as CO [64]. It can be seen from Figure 6C that, the initial potential for the MEO on the Pd@PdO-NiO_xH_y/C-400 catalyst is just -0.45 V, which is more negative compared to the other catalysts, meaning that methanol is oxidized more easily on the Pd@PdO-NiO_xH_y/C-400 catalyst than the other catalysts. The anode peak current densities for the MEO on the Pd/C, Pd-Ni/C, Pd-Ni/C-400, Pd@PdO-NiO_xH_y/C-300, Pd@PdO-NiO_xH_y/C-400 and Pd@PdO-NiO_xH_y/C-500 catalysts are 443.1, 828.1, 391.9, 978.9, 1118.9 and 119.3 mA mg⁻¹ Pd, respectively. As is shown in Figure 6D, moreover, the mass-specific current densities for the EEO on the Pd/C, Pd-Ni/C, Pd-Ni/C-400, Pd@PdO-NiO_xH_y/C-300, Pd@PdO-NiO_xH_y/C-400 and Pd@PdO-NiO_xH_y/C-500 catalysts are respectively up to 601.5, 961.9, 583.0, 1357.7, 1439.0, 156.5

mA mg⁻¹ Pd. For both the MEO and EEO, the Pd@PdO-NiO_xH_y/C-400 catalyst exhibits the highest electrocatalytic activities. Furthermore, the Pd@PdO-NiO_xH_y/C-400 catalyst also shows the most negative initial potential of -0.65 V for the EEO among these catalysts. The MEO and EEO activities of the Pd@PdO-NiO_xH_y/C-400 catalyst are about 2.5 and 1.4 times those of the Pd/C and Pd-Ni/C catalysts, respectively. These values are close to the corresponding ECSA ratios, suggesting that the ECSA is an important factor for enhancing the catalyst activity. It has been reported that, the PdO catalysts hardly have the electrocatalytic activity for the MEO [61]. Therefore, the active material in the Pd@PdO-NiO_xH_y/C-400 catalyst is not the PdO species in the PdO-NiO_xH_y shell layer, but the new Pd nanoparticles generated in the electrochemical activation. Firstly, the regenerated ultra-small Pd nanoparticles in the Pd@PdO-NiO_xH_y/C-400 catalyst prompt the catalyst surface to expose more active sites due to the size effect, which lead to the Pd@PdO-NiO_xH_y/C-400 catalyst exhibits large ECSA and excellent electrocatalytic performance [46,65]. Moreover, methanol and ethanol can be electrooxidized by NiO_xH_y, according to Equations 1 and 2 [45,66-68].

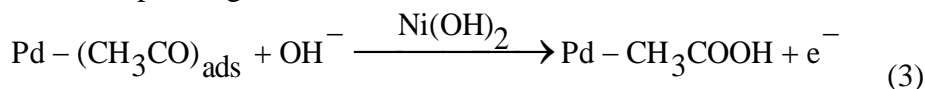


Firstly, NiOOH can be formed effectively through a combination of NiO_xH_y and OH⁻ in the solution, according to Equation 1 [45,66,67]. Then, methanol and ethanol can be electrooxidized by NiOOH in alkaline medium, according to Equation 2 [45,67,68].

According to Figures 6C and 6D, the catalytic activity of the Pd-Ni/C-400 catalyst is much lower than that of the Pd-Ni/C catalyst, suggesting that the formation of the alloying phase between the Pd and Ni components goes against the activity improvement of the Pd-Ni/C composite catalyst, which is agree with the previous report [62,63]. Compared Figure 6C with 6D, moreover, all the catalysts have a great increase in the mass current density of the oxidation peak for the EEO compared to the MEO, showing these Pd based catalysts are suited to electro-oxidize ethanol [69].

The CO-like tolerance of the Pt based catalyst for the MEO in acidic media is usually evaluated by the ratio between the forward (j_f) and backward (j_b) current densities, j_f/j_b [5,43,70]. Actually, this ratio is an approximate ratio between the areas of the anodic (A_a) and cathodic (A_c) polarization current peaks, A_a/A_c , because these current peaks have same peak shape and similar half peak width. This approximate disposal method is very common in the chromatographic analysis [71,72]. However, the CO-like tolerance of the Pd based catalyst in this work for the MEO and EEO in the alkaline electrolyte systems cannot be indexed using j_f/j_b , due to the great different peak shapes and half peak widths between the anodic and cathodic polarization current peaks. Therefore, A_a/A_c is employed to assess the CO-like tolerances of the Pd based catalysts for the MEO and EEO. According to Figure 6C, the A_a/A_c values for the MEO on the Pd/C, Pd-Ni/C, Pd-Ni/C-400, Pd@PdO-NiO_xH_y/C-300, Pd@PdO-NiO_xH_y/C-400 and Pd@PdO-NiO_xH_y/C-500 catalysts are 3.50, 4.12, 3.28, 3.76, 4.28 and 3.24, respectively. Correspondingly, the A_a/A_c values calculated from Figure 6D for the Pd/C, Pd-Ni/C, Pd-Ni/C-400, Pd@PdO-NiO_xH_y/C-300, Pd@PdO-NiO_xH_y/C-400 and Pd@PdO-NiO_xH_y/C-500 catalysts are respectively 1.66, 1.83, 1.48, 1.80, 1.73 and 1.71. It is found that, the Pd-Ni/C, Pd@PdO-NiO_xH_y/C-300 and Pd@PdO-NiO_xH_y/C-400 catalysts exhibit excellent CO-like tolerances for both the MEO and EEO. The increase in the CO tolerance of the Pd-Ni/C, Pd@PdO-NiO_xH_y/C-300 and Pd@PdO-NiO_xH_y/C-400 catalysts is closed associated with the bifunctional mechanism [4,5,7,64]. In

term of the Pd-Ni/C catalyst, the CO-like species on the Pd atoms are reacted with the OH_{ads} formed on the Ni atoms, due to its low oxidation potential [4,5,7,64]. For the Pd@PdO-NiO_xH_y/C-300 and Pd@PdO-NiO_xH_y/C-400 catalysts, the OH_{ads} species can also be produced on the surface of the metal oxides by the hydration of NiO_xH_y [45,73,74]. Therefore, the recovery of the Pd surface can be achieved by the reaction between the OH_{ads} on the surface of the Ni(OH)₂ species and the poisoning intermediates adsorbed on the active site of the catalyst [45,73,74]. Equations 3 and 4 can be used to explain the corresponding mechanism [74]:



For all the as-prepared catalysts, their CO-like tolerances for the MEO are about 2 times as high as those for the EEO, indicating that more CO-like species are produced during the EEO reaction compared to the MEO process. The reason is that the electron number transferred in the EEO (12) is more than that in the MEO (6).

In order to study the stability of the as-prepared catalysts, the chronoamperometry tests are carried out at -0.1 V vs. Ag|AgCl for 3600 s in the 0.1 M KOH + 1 M CH₃OH and 0.1 M KOH + 1 M CH₃CH₂OH mixed solutions, respectively. The corresponding chronoamperograms are revealed in Figure 7. As can be seen from Figure 7A, the stable current densities for the MEO on the Pd/C, Pd-Ni/C, Pd-Ni/C-400, Pd@PdO-NiO_xH_y/C-300, Pd@PdO-NiO_xH_y/C-400 and Pd@PdO-NiO_xH_y/C-500 catalysts respectively are 2.93, 7.25, 4.43, 8.37, 12.57, 0.35 mA mg⁻¹ Pd; while their stable mass-specific activities for the EEO respectively reach to 16.75, 31.94, 18.48, 66.05, 86.35, 2.30. Apparently, the Pd@PdO-NiO_xH_y/C-400 catalyst exhibits much higher stable current densities for both the MEO and EEO, compared to other catalysts. Moreover, the variation regular for the durability of the catalysts is similar to the activity change law for both the MEO and EEO. For the MEO, the stable current density of the Pd@PdO-NiO_xH_y/C-400 catalyst is about 1.7 and 4.3 times those of the Pd-Ni/C and Pd/C catalysts, respectively. The stable current density for the EEO on the Pd@PdO-NiO_xH_y/C-400 catalyst is also much higher than those of the other catalysts. By comparing the Pd@PdO-NiO_xH_y/C-400 catalyst with the Pd-Ni/C and Pd/C catalysts, the corresponding ratios of the stable current density for the EEO reach to 2.7 and 5.2, respectively. The improvement in the electrocatalytic stability of the Pd@PdO-NiO_xH_y/C-400 catalyst is also relevant to its composition and structure. Firstly, the newly Pd nanoparticles with ultra-small size hardly becomes big in the electrochemical reaction, since they are divided by the NiO_xH_y species. The recovery of the Pd surface, additionally, which is resulted from the electrooxidation of the CO-like species under the influence of the OH_{ads} on the surface of the NiO_xH_y species, due to the bifunctional mechanism, is another factor [45,73,74]. However, the stable current density of the Pd@PdO-NiO_xH_y/C-500 catalyst is greatly reduced, which is probably caused by the abscission of the Pd@PdO-NiO_xH_y nanoparticles with big size from the carbon support. Surprisingly, the stable current densities on all the as-prepared catalysts for the EEO are much higher than those for the MEO. Furthermore, the stable current density ratio (6.9) between the EEO and MEO on the Pd@PdO-NiO_xH_y/C-400 catalyst is far more than the corresponding anodic current density ratio (1.3) revealed in Figures 6C and 6D, although the Pd@PdO-NiO_xH_y/C-400 catalyst reveals a better CO tolerance for the MEO compared to the EEO. The possible reason is that,

the poisoning species produced during the EEO can be desorbed more easily than that formed during the MEO. These results imply that the Pd@PdO-NiO_xH_y/C catalyst has broad application prospects in the field of the DAFCs.

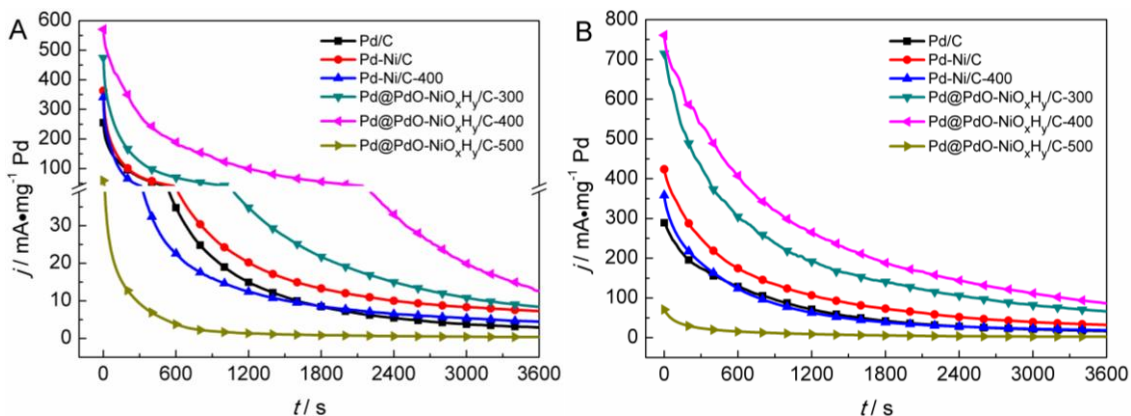


Figure 7. Chronoamperograms collected for 3600 s at -0.1 V vs. Ag|AgCl on the Pd/C, Pd-Ni/C, Pd-Ni/C-400, Pd@PdO-NiO_xH_y/C-300, Pd@PdO-NiO_xH_y/C-400 and Pd@PdO-NiO_xH_y/C-500 catalysts in 0.1 M KOH solutions respectively with 1 M CH₃OH (A) and 1 M CH₃CH₂OH (B). All the currents are normalized using the Pd loading determined by ICP-MS.

4. CONCLUSION

The two-stage atomic rearrangements occurred in the Pd-Ni/C catalyst greatly improve its electrochemical performance. Firstly, the Pd and Ni atoms in the Pd-Ni/C catalyst are rearranged by heat treatment in a vacuum condition to prepare the Pd@PdO-NiO_xH_y/C catalyst. Then, the rearrangement of the Pd atoms in the Pd@PdO-NiO_xH_y nanoparticles is achieved through the electrochemical activation process. The TEM results of the Pd@PdO-NiO_xH_y/C-400 catalyst show that the Pd@PdO-NiO_xH_y nanoparticles are uniformly dispersed on the carbon support with an average particle diameter of 5.06 nm. The EDS mapping images, as well as the XRD and XPS results indicate that, only partial Pd atoms at the center of the Pd@PdO-NiO_xH_y nanoparticles in the Pd@PdO-NiO_xH_y/C-400 catalyst are kept as the metallic state. Furthermore, these Pd cores are completely encapsulated by NiO_xH_y doped PdO, forming a core-shell structure. The unique doped structure between NiO_xH_y and PdO in the Pd@PdO-NiO_xH_y nanoparticles, makes the new Pd nanoparticles formed by the rearrangement of the Pd atoms during the electrochemical activation, be separated by NiO_xH_y species, leading to they have ultra-small size. The ultra-small size of the newly generated Pd nanoparticles is favorable for the enhancement of its electrochemical activity, due to the size effect. Moreover, NiO_xH_y species around the newly formed Pd nanoparticles in the catalyst prevent them from becoming big, benefiting the improvement of its stability. The electrochemical measurements show that the Pd@PdO-NiO_xH_y/C-400 catalyst has the largest ECSA, highest catalytic activity and stability among these catalysts, due to its newly formed Pd nanoparticles with ultra-small size, unique doped structure between NiO_xH_y and PdO, as well as the bifunctional mechanism caused by NiO_xH_y.

Furthermore, the stable current density on the Pd@PdO-NiO_xH_y/C-400 catalyst for the EEO is 6.9 times that for the MEO, implying that the Pd@PdO-NiO_xH_y/C catalyst has broad application prospects in the field of the EEO. In addition, it will be a promising approach adding transition metals and controlling the formation of metal oxides and hydroxides in nanoscale to improve the performance of all the noble metal-based nanocatalysts.

ACKNOWLEDGEMENT

This work is supported by the Major Science and Technology Project of Shanxi Province (20181102019).

References

1. C. D. Dong, C. W. Chen, C. F. Chen and C. M. Hung, *Sci. Rep.*, 4 (2014) 5790.
2. I. H. Hafez, M. R. Berber, T. Fujigaya and N. Nakashima, *Sci. Rep.*, 4 (2014) 6295.
3. J. E. Sulaiman, S. Zhu, Z. Xing, Q. Chang and M. Shao, *ACS Catal.*, 7 (2017) 5134.
4. A. B. A. A. Nassr, I. Sinev, M. P. W. Grünert and M. Bron, *ACS Catal.*, 4 (2014) 2449.
5. J. E. Robinson, N. Y. Labrador, H. Chen, B. E. Sartor and D. V. Esposito, *ACS Catal.*, 8 (2018) 11423.
6. N. H. Kwon, M. Kim, X. Jin, J. Lim, I. Y. Kim, N. S. Lee, H. Kim and S. J. Hwang, *NPG Asia Mater.*, 10 (2018) 659.
7. R. S. Amin, R. M. Abdel Hameed, K. M. El-Khatib and M. Elsayed Youssef, *Int. J. Hydrogen Energy*, 39 (2014) 2026.
8. H. Zhong, K. Li, Q. Zhang, J. Wang, F. Meng, Z. Wu, J. Yan and X. Zhang, *NPG Asia Mater.*, 8 (2016) e308.
9. Y. Zheng, Y. Jiao, Y. Zhu, Q. Cai, A. Vasileff, L. H. Li, Y. Han, Y. Chen and S. Z. Qiao, *J. Am. Chem. Soc.*, 139 (2017) 3336.
10. H. Yang, J. Liu, J. Wang, C. K. Poh, W. Zhou, J. Lin and Z. Shen, *Electrochim. Acta*, 2016;216:246-52.
11. R. Cui, L. Mei, G. Han, J. Chen, G. Zhang, Y. Quan, N. Gu, L. Zhang, Y. Fang, B. Qian, X. Jiang and Z. Han, *Sci. Rep.*, 7 (2018) 41826.
12. Y. H. Cho, B. Choi, Y. H. Cho, H. S. Park and Y. E. Sung, *Electrochem. Commun.*, 9 (2007) 378.
13. Y. Feng, D. Bin, B. Yan, Y. Du, T. Majima and W. Zhou, *J. Colloid Interface Sci.*, 493 (2017) 190.
14. C. Zhu, D. Wen, M. Oschatz, M. Holzschuh, W. Liu, A. K. Herrmann, F. Simon, S. Kaskel and A. Eychmüller, *Small*, 11 (2015) 1430.
15. Z. Cao, Q. Chen, J. Zhang, H. Li, Y. Jiang, S. Shen, G. Fu, B. Lu, Z. Xie and L. Zheng, *Nat. Commun.*, 8 (2017) 15131.
16. L. Shen, H. Li, L. Lu, Y. Luo, Y. Tang, Y. Chen and T. Lu, *Electrochim. Acta*, 89 (2013) 497.
17. Y. Wang, Y. Zhao, J. Yin, M. Liu, Q. Dong and Y. Su, *Int. J. Hydrogen Energy*, 39 (2014) 1325.
18. X. Lu, L. Zheng, M. Zhang, H. Tang, X. Li and S. Liao, *Electrochim. Acta*, 238 (2017) 194.
19. Q. Dong, Y. Zhao, X. Han, Y. Wang, M. Liu and Y. Li, *Int. J. Hydrogen Energy*, 39 (2014) 14669.
20. Q. He, W. Chen, S. Mukerjee, S. Chen and F. Laufek, *J. Power Sources*, 187 (2009) 298.
21. B. M. Hunter, W. Hieringer, J. R. Winkler, H. B. Gray and A. M. Müller, *Energy Environ. Sci.*, 9 (2016) 1734.
22. X. Jin, J. Lim, N. S. Lee and S. J. Hwang, *Electrochim. Acta*, 235 (2017) 720.
23. M. Zhang, Z. Yan, Q. Sun, J. Xie and J. Jing, *New J. Chem.*, 36 (2012) 2533.
24. F. Li, Y. Guo, R. Li, F. Wu, Y. Liu, X. Sun, C. Li, W. Wang and J. Gao, *J. Mater. Chem. A*, 1 (2013) 6579.
25. R. Awasthi and R. N. Singh, *Int. J. Hydrogen Energy*, 37 (2012) 2103.

26. S. Alayoglu, A. U. Nilekar, M. Mavrikakis and B. Eichhorn, *Nat. Mater.*, 7 (2008) 333.
27. J. F. Weaver, *Chem. Rev.*, 113 (2013) 4164.
28. C. Hakanoglu, J. M. Hawkins, A. Asthagiri and J. F. Weaver, *J. Phys. Chem. C*, 114 (2010) 11485.
29. J. A. Jr. Hinojosa, H. H. Kan and J. F. Weaver, *J. Phys. Chem. C*, 112 (2008) 8324.
30. A. L. Gerrard, J. J. Chen and J. F. Weaver, *J. Phys. Chem. B*, 109 (2005) 8017.
31. C. Tang, H. F. Wang, X. L. Zhu, B. Q. Li and Q. Zhang, *Part. Part. Syst. Charact.*, 33 (2016) 473.
32. J. Wu, Z. Ren, S. Du, L. Kong, B. Liu, W. Xi, J. Zhu and H. Fu, *Nano Research*, 9 (2016) 713.
33. J. Rossmeisl, A. Logadottir and J. K. Nørskov, *Chem. Phys.*, 319 (2005) 178.
34. J. Rossmeisl, Z. W. Qu, H. Zhu, G. J. Kroes and J. K. Nørskov, *J. Electroanal. Chem.*, 607 (2007) 83.
35. X. Huang and M. J. Beck, *ACS Catal.*, 5 (2015) 6362.
36. C. S. Sharma, A. S. K. Sinha, R. N. Singh, *Int. J. Hydrogen Energy*, 39 (2014) 20151.
37. Z. Zhao, H. Liu, W. Gao, W. Xue, Z. Liu, J. Huang, X. qing Pan and Y. Huang, *J. Am. Chem. Soc.*, 140 (2018) 9046.
38. C. Wang, L. Zhang, H. Yang, J. Pan, J. Liu, C. Dotse, Y. Luan, R. Gao, C. Lin, J. Zhang, J. P. Kilcrease, X. Wen, S. Zou and J. Fang, *Nano Lett.*, 17 (2017) 2204.
39. V. Beermann, M. Gocyla, S. Köhl, E. Padgett, H. Schmies, M. Goerlin, N. Erini, M. Shviro, M. Heggen, R. E. Dunin-Borkowski, D. A. Muller and P. Strasser, *J. Am. Chem. Soc.*, 139 (2017) 16536.
40. V. Beermann, S. Köhl and P. Strasser, *J. Electrochem. Soc.*, 165 (2018) J3026.
41. X. Tuaeov, S. Rudi, V. Petkov and A. Hoell, *ACS Nano*, 7 (2013) 5666.
42. L. Lu, J. Wang, L. Guo, X. Zhao, Y. Zhang, Y. Yang and S. Yan, *Int. J. Electrochem. Sci.*, 14 (2019) 6546.
43. S. Yan, S. Zhang, W. Zhang, J. Li, L. Gao, Y. Yang and Y. Gao, *J. Phys. Chem. C*, 118 (2014) 29845.
44. S. Yan, L. Gao, S. Zhang, W. Zhang, Y. Li and L. Gao, *Electrochim. Acta*, 94 (2013) 159.
45. S. Yan, L. Gao, S. Zhang, L. Gao, W. Zhang and Y. Li, *Int. J. Hydrogen Energy*, 38 (2013) 12838.
46. S. Yan and S. Zhang, *Int. J. Hydrogen Energy*, 36 (2011) 13392.
47. Z. Yan, Z. Hu, C. Chen, H. Meng, P. K. Shen, H. Ji and Y. Meng, *J. Power Sources*, 195 (2010) 7146.
48. X. Ren, M. Huang, S. Luo, Y. Li, L. Deng, H. Mi, L. Sun and P. Zhang, *J. Mater. Chem. A*, 6 (2018) 10856.
49. F. Kadirgan, A. M. Kannan, T. Atilan, S. Beyhan, S. S. Ozenler, S. Suzer, *Int. J. Hydrogen Energy*, 2009;34:9450-60.
50. K. Arora and N. K. Puri, *Vacuum*, 154 (2018) 302.
51. Y. Zhou, C. Du, G. Han, Y. Gao and G. Yin, *Electrochim. Acta*, 217 (2016) 203.
52. M. C. Biesinger, B. P. Payne, L. W. M. Lau, A. Gerson and R. S. C. Smart, *Surf. Interface. Anal.*, 41 (2009) 324.
53. A. P. Grosvenor, M. C. Biesinger, R. S. C. Smart and N. S. McIntyre, *Surf. Sci.*, 600 (2006) 1771.
54. Y. Zhao, Y. E. L. Fan, Y. Qiu and S. Yang, *Electrochim. Acta*, 52 (2007) 5873.
55. N. Spinner and W. E. Mustain, *Electrochim. Acta*, 56 (2011) 5656.
56. M. Wang, W. Liu and C. Huang, *Int. J. Hydrogen Energy*, 34 (2009) 2758.
57. Q. Xue, J. Bai, C. Han, P. Chen, J. X. Jiang and Y. Chen, *ACS Catal.*, 8 (2018) 11287.
58. Q. Tan, C. Shu, J. Abbott, Q. Zhao, L. Liu, T. Qu, Y. Chen, H. Zhu, Y. Liu, G. Wu, *ACS Catal.*, 9 (2019) 6362.
59. L. Chen, H. Guo, T. Fujita, A. Hirata, W. Zhang, A. Inoue, M. Chen, *Adv. Funct. Mater.*, 21 (2011) 4364.
60. J. N. Zheng, M. Zhang, F. F. Li, S. S. Li, A. J. Wang and J. J. Feng, *Electrochim. Acta*, 130 (2014) 446.
61. C. S. Chen and F. M. Pan, *J. Power Sources*, 208 (2012) 9.

62. J. R. Kitchin, J. K. Nørskov, M. A. Barteau and J. G. Chen, *Phys. Rev. Lett.*, 93 (2004) 156801.
63. M. Mavrikakis, B. Hammer and J. K. Nørskov, *Phys. Rev. Lett.*, 81 (1998) 2819.
64. F. Ren, C. Wang, C. Zhai, F. Jiang, R. Yue, Y. Du, P. Yang and J. Xu, *J. Mater. Chem. A*, 1, (2013) 7255.
65. Y. Kim and D. H. Kim, *Appl. Catal. B-Environ.*, 244 (2019) 684.
66. C. Xu, Y. Hu, J. Rong, S. Jiang and Y. Liu, *Electrochem. Commun.*, 9 (2007) 2009.
67. M. A. Abdel Rahim, R. M. Abdel Hameed and M. W. Khalil, *J. Power Sources*, 134 (2004) 160.
68. K. W. Park, J. H. Choi, B. K. Kwon, S. A. Lee, Y. E. Sung, H. Y. Ha, S. A. Hong, H. Kim A. Wieckowski, *J. Phys. Chem. B*, 106 (2002) 1869.
69. M. Zhang, Z. Yan and J. Xie, *Electrochim. Acta*, 77 (2012) 237.
70. A. M. Hofstead-Duffy, D. J. Chen, S. G. Sun and Y. J. Tong, *J. Mater. Chem.*, 22 (2012) 5205.
71. D. Nieć and P. K. Kunicki, *J. Chromatogr. B*, 1002 (2015) 63.
72. H. Cheng, C. Wu, L. Shen, J. Liu and Z. Xu, *Anal. Chim. Acta*, 828 (2014) 9.
73. C. Xu, P. K. Shen and Y. Liu, *J. Power Sources*, 164 (2007) 527.
74. Z. Zhang, L. Xin, K. Sun and W. Li, *Int. J. Hydrogen Energy*, 36 (2011) 12686.

© 2020 The Authors. Published by ESG (www.electrochemsci.org). This article is an open access article distributed under the terms and conditions of the Creative Commons Attribution license (<http://creativecommons.org/licenses/by/4.0/>).